Invited Article: CARS molecular fingerprinting using sub-100-ps microchip laser source with fiber amplifier

Invited Article: CARS molecular fingerprinting using sub-100-ps microchip laser source with fiber amplifier

Hiroaki Yoneyama, Kazuhiro Sudo, Philippe Leproux, Vincent Couderc, Akihito Inoko, and Hideaki Kano

Invited Article: CARS molecular fingerprinting using sub-100-ps microchip laser source with fiber amplifier

Hiroaki Yoneyama,[1] Kazuhiro Sudo,[2] Philippe Leproux,[3,4] Vincent Couderc,[3] Akihito Inoko,[5] and Hideaki Kano[1,6,7,a]

[1]*Department of Applied Physics, Graduate School of Pure and Applied Sciences, University of Tsukuba, 1-1-1 Tennodai, Tsukuba, Ibaraki 305-8573, Japan*
[2]*RIKEN BioResource Center, 3-1-1 Koyadai, Tsukuba, Ibaraki 305-0074, Japan*
[3]*Institut de Recherche XLIM, UMR CNRS No. 7252, 123 Avenue Albert Thomas, 87060 Limoges Cedex, France*
[4]*LEUKOS, 37 Rue Henri Giffard, 87280 Limoges, France*
[5]*Division of Cancer Epidemiology and Prevention, Aichi Cancer Center Research Institute, 1-1 Kanokoden, Chikusa-ku, Nagoya, Aichi 464-8681, Japan*
[6]*Institute of Applied Physics, University of Tsukuba, 1-1-1 Tennodai, Tsukuba, Ibaraki 305-8573, Japan*
[7]*Tsukuba Research Center for Energy Materials Science (TREMS), University of Tsukuba, 1-1-1 Tennodai, Tsukuba, Ibaraki 305-8571, Japan*

We have developed an ultrabroadband multiplex coherent anti-Stokes Raman scattering (CARS) microspectroscopic system using a supercontinuum (SC) seeded by sub-100-ps (85 ps) laser pulses with a sub-MHz (0.82 MHz) repetition rate. Because of the high peak power and ultrabroadband spectral profile of the SC, we can efficiently generate multiplex CARS signals in the spectral range of 600–3600 cm^{-1}, which covers the entire molecular fingerprint region, as well as the C—H and O—H stretching regions. Due to the high peak power of the new laser source, the exposure time (pixel dwell time) for CARS imaging of polymer beads was reduced to less than 1 ms (0.8 ms), which was limited by the readout time of a CCD camera. Owing to the improvement in CARS spectral quality, clear molecular fingerprinting was achieved for living HeLa cells at different phases in the cell cycle. © *2018 Author(s). All article content, except where otherwise noted, is licensed under a Creative Commons Attribution (CC BY) license (http://creativecommons.org/licenses/by/4.0/).* https://doi.org/10.1063/1.5027006

INTRODUCTION

Nonlinear Raman spectroscopic imaging is a powerful method of performing label-free microscopic molecular imaging.[1–6] Coherent anti-Stokes Raman scattering (CARS) and stimulated Raman scattering (SRS) are two of the major techniques of nonlinear Raman spectroscopic imaging. Several spectroscopic methods based on the CARS and SRS techniques have been reported, including the so-called multiplex method, in which a broadband laser source is used for multiple excitations of the vibrational modes.[7–13] Another method involving rapid alteration of the laser-beam wavelength in each frame[14–18] and another approach involving Fourier-transform CARS techniques[19–21] have been reported. In addition to these techniques, the frequency comb technique has also been applied to CARS microspectroscopy.[22] Among these methods, multiplex CARS[7–11] can provide an ultrabroadband spectral coverage of ~3000 cm^{-1}, which spans the entire region of the fundamental vibrational modes.[23] In this technique, a single mode-locked broadband laser source[24,25] or a master laser source combined with supercontinuum (SC) radiation[9,10] has been used. In the latter case, the SC can be generated by seeding a portion of the master laser output into a tapered fiber[9] or a photonic crystal fiber (PCF).[10] Recently, a sub-nanosecond laser source has also been used as the master laser source

---

[a]Electronic mail: hkano@bk.tsukuba.ac.jp.

to generate SC for nonlinear Raman spectroscopic imaging.[26] Through imaging based on the multi-modal channels of the multiplex CARS and second and third harmonic generations (SHG and THG, respectively) using the sub-nanosecond laser source, the filamentous protein known as Rootletin[27] was found to be SHG-active.[28] Furthermore, the mouse parietal bone has been visualized using epi-detected multiplex CARS with a short pixel dwell time of 5 ms.[29] In order to further improve the multiplex CARS microspectroscopic system, optimization of the peak intensity and repetition rate of the laser source must be considered key factors.

In the present study, we introduce a new laser source based on a microchip oscillator and fiber amplifier to ultrabroadband multiplex CARS microspectroscopy. The exposure time (pixel dwell time) was shortened to less than 1 ms (0.8 ms), limited by the readout time of a CCD camera due to the high peak power of the new laser source. Broadband (spectral coverage: 200–1500 cm^{-1}) CARS spectroscopy at a record scan rate of 24 000 spectra/s[20] and ultrabroadband (spectral coverage: 500–3500 cm^{-1}) multiplex CARS microspectroscopy at 3.5 ms exposure[13] have been reported. On the other hand, this protocol with an exposure of less than 1 ms (spectral coverage: 600–3600 cm^{-1}) is, to the best of our knowledge, the fastest in ultrabroadband multiplex CARS microspectroscopy.

EXPERIMENTAL SETUP

Multiplex CARS microspectroscopic system

A schematic of our experimental setup is shown in Fig. 1(a). The laser source is based on a master oscillator fiber amplifier (MOFA) configuration, involving a microchip oscillator and an Yb-doped fiber amplifier (SM-1000, Leukos, France, custom-made). The microchip oscillator is a passively Q-switched laser comprising a Nd:YVO$_4$ crystal bonded with a saturable absorber mirror and pumped at 808 nm. The fiber amplifier is based on a two-stage configuration including a pre-amplifier and a booster using a polarization-maintaining, large-mode-area, double-clad Yb-doped fiber. The wavelength, temporal duration, and repetition rate are 1064 nm, 85 ps, and 0.82 MHz, respectively. The repetition rate of the laser source is more than one order higher than that of the previous system[23] (0.033 MHz), enabling us to develop a fast-scanning microscope. The laser pulses are divided into two with one part being used as the pump radiation (ω_1) for the CARS process and the other being seeded into a PCF to generate a SC, which is used as the Stokes radiation (ω_2) for the CARS process. The cross section of the PCF is shown in Fig. 1(a). We used dielectric mirrors and silver mirrors for the propagation of the ω_1 and ω_2 pulses, respectively. The SC radiation is collimated by an off-axis parabolic mirror (RC04APC-P01, Thorlabs) to suppress the chromatic aberration. The spectral profile of the SC after the off-axis parabolic mirror [Fig. 1(b)] was measured by using a near-infrared (NIR) spectrometer (FT-NIR Rocket, ARCoptix S.A., Switzerland). Since the spectral density around NIR should be high for efficient CARS signal generation, the PCF was fabricated to efficiently generate the spectral components between 1100 and 1700 nm. The pulse energies of the ω_1 and ω_2 pulses were approximately 2 and 1 μJ, respectively, corresponding to peak powers of approximately 24 and 12 kW. In comparison with our previous setup[23] involving longer pulses (~1 ns), the peak powers in the present study were approximately ~3.4 and ~5 times larger than those in the previous study (7 and 2.4 kW for the w1 and w2 pulses, respectively), respectively. After removing the spectral components shorter than 1064 nm from the SC using a long-pass filter, the ω_1 and ω_2 laser pulses were superimposed by using an edge filter, guided with silver mirrors and then introduced into a modified inverted microscope (ECLIPSE Ti-U, Nikon, Japan). Incident laser pulses were tightly focused onto a sample by the first objective lens (CFI Plan Apo 60× NA 1.27, Nikon, Japan). The sample was placed on a piezoelectric stage (Nano-LP200, Mad City Lab, WI) for microscopic imaging, and the CARS signal was collected by using the second objective lens (Plan S Fluor 40× NA 0.6, Nikon, Japan) and was dispersed by using the spectrometer (LS-785, Princeton Instruments, MA). Finally, the CARS signal was detected by using the CCD camera (Blaze 400-HR for polymer-bead imaging and PIXIS 100-BR-DD for living-cell imaging, Princeton Instruments, MA). Although the microscope objective for laser focusing has chromatic aberration in the NIR region, the signal is generated only from the spatially overlapped area of ω_1 (1064 nm, monochromatic) and ω_2 (SC). Since the ω_1 laser beam is monochromatic and tightly
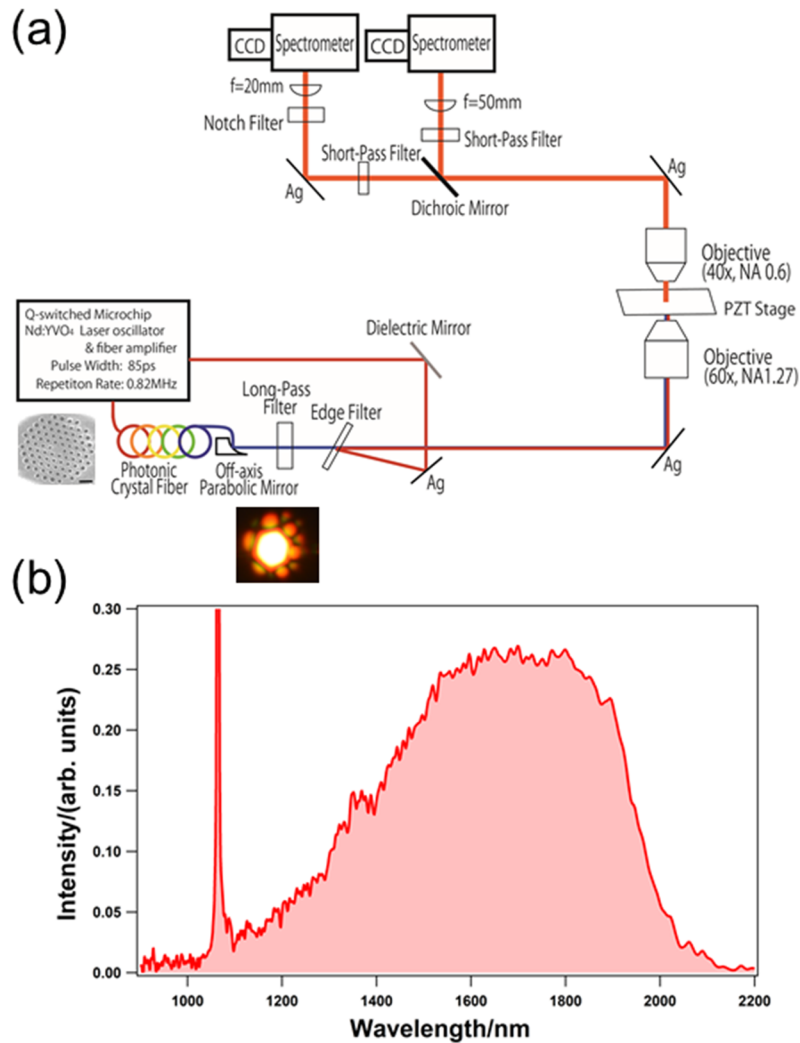
FIG. 1. (a) Schematic of the experimental setup of the ultrabroadband multiplex CARS microspectroscopic system using a sub-100-ps laser source. The photo of the PCF cross section (scale bar: 5 μm) and the far-field output pattern of the SC are also shown; (b) spectral profile of SC radiation after the off-axis parabolic mirror. Intensity correction of the spectrometer was not performed.

focused on the sample, the wavelength dependence of the focusing properties of SC was not critical in the present study.

To confirm the performance of the developed system, polystyrene beads were subjected to CARS imaging as test samples. Polystyrene beads (diameter 10 μm) were purchased from Polysciences, Inc. (Warrington, PA, USA). The original aqueous suspension of the beads was first diluted more than 10-times, and approximately 50 μl of the suspension was sandwiched between a cover glass and a slide glass. Figure 2(a) shows the raw CARS spectrum of the polystyrene bead without intensity correction. The input laser power was about 90 mW in total (ω_1 and ω_2). Although the exposure time per image pixel was set at 0 ms in the software, the CARS signal was accumulated within the finite readout time of ~0.8 ms. Therefore, the effective exposure time was estimated to be ~0.8 ms.

HeLa cells

HeLa cells were provided by the RIKEN Bio-resource Center, maintained in a minimum essential medium supplemented with 10% fetal bovine serum (FBS) at 37 °C in a humidified incubator containing 5% CO_2. Cell passages were performed every 3–4 days. For the CARS study, coverslips were settled in culture dishes, onto which the HeLa cells were then seeded. One day after cell seeding,
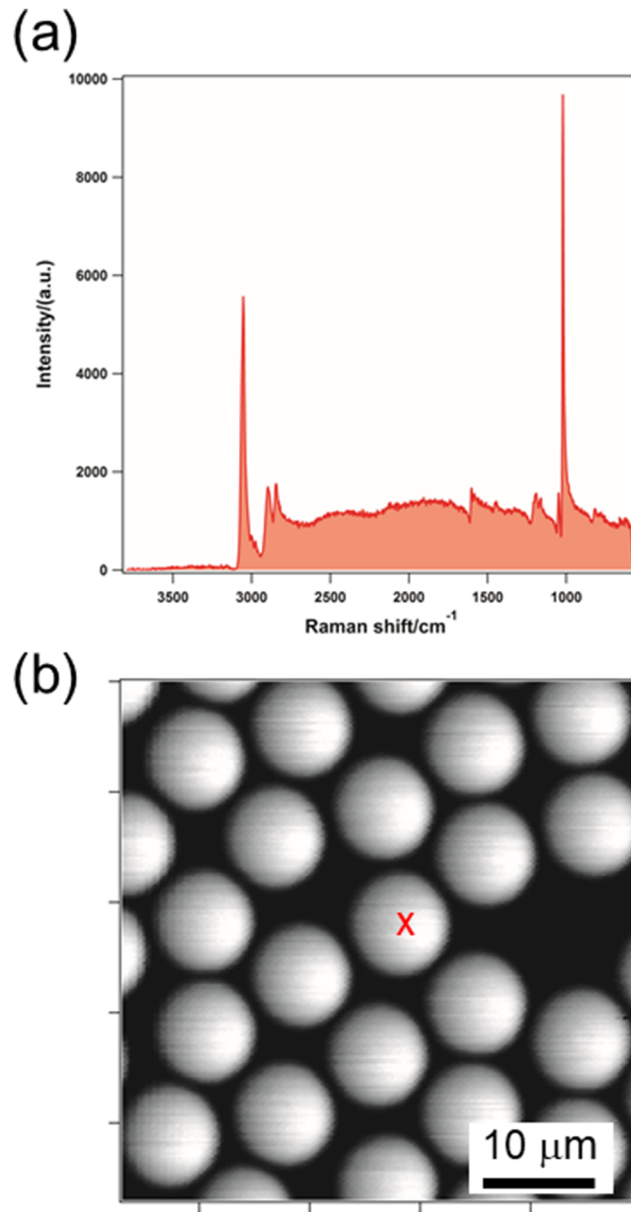
FIG. 2. (a) Raw CARS spectrum (intensity-uncorrected) of the polystyrene beads at the position of the red cross in (b). The effective exposure time was 0.8 ms; (b) CARS image of polystyrene beads at the phenyl ring breathing mode (1003 cm^{-1}) for effective exposure time of 0.8 ms.

the coverslips were removed from the culture dishes, put on glass slides, and sealed with nail varnish just before measurements. The input laser power and the exposure time per image pixel (pixel dwell time) were set at ~200 mW in total and 50 ms, respectively, to obtain CARS spectra with a high signal-to-noise ratio. Based on the optical images, we confirmed that laser irradiation produced no substantial morphological change in cells.

NIH-3T3 cells

NIH-3T3 cells were purchased from ATCC (Manassas, VA). The cells were seeded onto coverslips and cultured in Dulbecco's modified Eagle's medium supplemented with 10% FBS. The sample preparation was the same as that for the HeLa cells. The input laser power and the exposure time per image pixel (pixel dwell time) were set at ~200 mW in total and 10 ms, respectively.

RESULTS AND DISCUSSION

HeLa cells in G1 phase

Figure 2 shows the intra-cellular averaged Im[$\chi^{(3)}$] spectrum of a HeLa cell in the G1 phase. The Im[$\chi^{(3)}$] spectrum at each spatial position was calculated from the raw CARS spectra using the maximum entropy method (MEM).[23,30] The MEM does not require any *a priori* knowledge of the vibrational bands but can still retrieve the phase information on the third-order nonlinear susceptibility $\chi^{(3)}$, the imaginary part of which corresponds to the ordinary (spontaneous) Raman spectrum.[30] Therefore, the amplitude of the retrieved signal, Im[$\chi^{(3)}$], is proportional to molecular concentration. The CARS signal was clearly observed between 600 and 3200 cm^{-1}. We performed a denoising procedure using a singular value decomposition analysis.[23] The assignments of the corresponding vibrational bands are listed in Table I. By analyzing the spectral profile at each cell position, we reconstructed CARS images for the various Raman bands. Figure 3 summarizes the results of ultrabroadband multiplex CARS imaging, where Figs. 3(a)–3(j) show the CARS images at 3063, 3010, 2930, 2851, 1738, 1574, 1098, 1004, 791, and 719 cm^{-1}, respectively. In addition, SHG

TABLE I. Vibrational bands and their assignments for the intracellular Im[$\chi^{(3)}$] spectrum.[31–39] stretch.: stretching; deform.: deformation; rock.: rocking; twist.: twisting; scis.: scissors; bend.: bending; sym.: symmetric; asym.: asymmetric; deg.: degenerate; breath.: breathing; bk.: DNA backbone; A: adenine; C: cytosine; G: guanine; T: thymine; U: uracil; Phe: phenylalanine; Trp: tryptophan; Tyr: tyrosine.

| Typical Raman shift values (cm^{-1})	Assignment	Main molecular components
3060	C−H stretch. (aromatic)	Proteins
3010	=C−H stretch.	Lipids
2930	CH$_3$ sym. stretch.	Proteins/lipids
2880	Overtone of CH$_3$ asym. deform. In fermi resonance with CH$_3$ sym. stretch./CH$_2$ asym. stretch.	Proteins/lipids
2850	CH$_2$ sym. stretch.	Lipids
2580	S−H stretch.	Proteins
1741	C=O stretch. (ester)	Lipids
1655	*cis* C=C stretch./Amide I	Lipids/proteins
1611	Tyr, Trp	Proteins
1602	Phe	Proteins
1574	Purine ring (A and G)	DNAs and RNAs
1481	Purine ring (A and G)	DNAs and RNAs
1452	CH$_3$ deg. deform.	Proteins
1438	CH$_2$ scis.	Lipids
1376	T, A, and C	DNAs
1340	CH deform.	Proteins
1335	Purine ring (A and G)	DNAs and RNAs
1300	CH$_2$ twist.	Lipids
1260	=C−H bend.	Lipids
1240	Amide III	Proteins
1205	C−C$_6$H$_5$ (phenyl ring) stretch.	Proteins
1130	Skeletal C−C (*trans*) stretch.	Lipids
1097	PO$_2^-$ stretch.	DNAs and RNAs
1084	Skeletal C−C (*gauche*) stretch.	Lipids
1063	Skeletal C−C (*trans*) stretch.	Lipids
1030	In-plane phenyl ring deform.	Proteins
1004	Phenyl ring breath.	Proteins
939	C−C	Proteins
892	C$_2$−C$_1$ (*trans*) stretch./CH$_3$ rock.	Lipids
876	C$_2$−C$_1$ (*gauche*) stretch./CH$_3$ rock.	Lipids
791	Pyrimidine ring (C, T, and U)/bk. (O-P-O)	DNAs and RNAs
726	CH$_2$ rock.	Lipids
719	Head group (choline (H$_3$C)N$^+$ sym. stretch.) of phosphatidylcholine	Lipids
709	Cholesterol	Lipids
660	C−S stretch.	Proteins
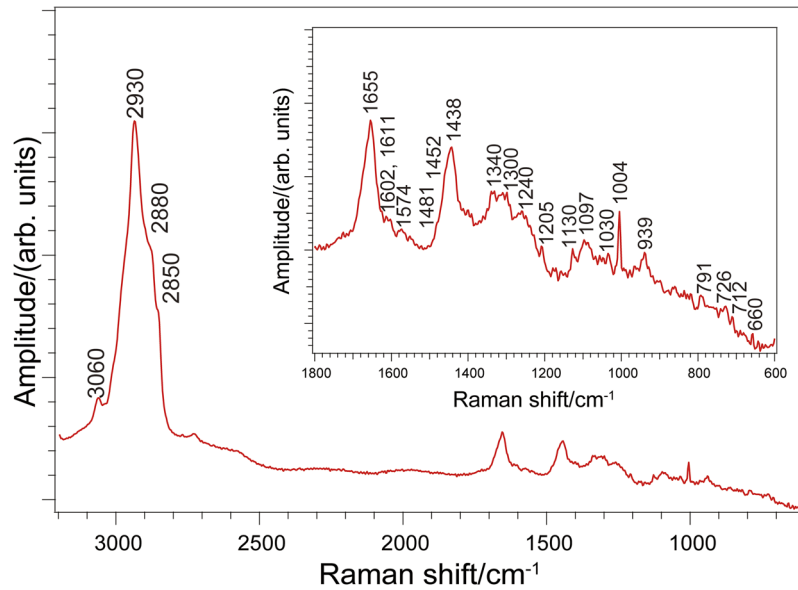
FIG. 3. Intracellular-averaged Im[$\chi^{(3)}$] spectrum of a HeLa cell in the G1 phase.

and THG images are shown in Figs. 3(k) and 3(l), respectively. It is apparent that the microscopic intracellular structures were successfully visualized based on their molecular fingerprint. In particular, particle-like structures with diameters of a few micrometers are shown in Figs. 3(b)–3(e) and 3(l). The C—H stretching vibrational mode of the =C—H bonds, CH_3 stretching vibrational mode, CH_2 stretching vibrational mode, and C=O stretching vibrational mode due to esters were assigned to the CARS images in Figs. 3(b)–3(e), respectively, all of which are typically found in lipid spectra. Thus, we safely identified the particle-like structures as intracellular lipid droplets. The CARS image at 2930 cm^{-1}, due to the CH_3 stretching vibrational mode, exhibits a relatively dark and circular region near the center of the cell, corresponding to the cell nucleus, and the organelles inside the cell nucleus correspond to nucleoli. High image contrast is obtained for the nucleoli in Figs. 3(a), 3(c), and 3(f)–3(i). The aromatic C—H stretching vibrational mode, purine ring stretching vibrational mode due to adenine and guanine, PO_2^- stretching vibrational mode due to DNA, phenyl ring breathing vibrational mode, and pyrimidine ring vibrational mode due to cytosine, thymine, and uracil were assigned to the CARS images in Figs. 3(a) and 3(f)–3(i), respectively. These bands originate mainly from proteins and DNAs.

In order to investigate the intra-cellular molecular distribution in greater detail, we analyzed the intracellular spatially resolved Im[$\chi^{(3)}$] spectra; the results are summarized in Fig. 5. The areas marked by the blue and red frames in Fig. 5(a) correspond to a lipid droplet and nucleoli, respectively, the Im[$\chi^{(3)}$] spectra of which are shown in Fig. 5(b). In comparison with Fig. 3, which presents a whole-cell-averaged spectral profile, lipid-rich and DNA/RNA-rich spectra are apparent at the areas corresponding to the lipid droplet (blue) and nucleoli (red) in Fig. 5(b). In particular, the vibrational bands at 1084 and 1096 cm^{-1}, identified as C—C (*gauche*) stretching and PO_2^- stretching, respectively, are clearly distinguishable in the Im[$\chi^{(3)}$] spectra. The vibrational bands at 1655 cm^{-1} in the two spectra have different bandwidths because each band mainly originates from different molecular species (lipids and proteins). The vibrational band due to *cis* C=C stretching [blue spectrum, Fig. 5(b)] is typically narrower than that due to amide I [red spectrum, Fig. 5(b)]. Moreover, the spectral profile at the lipid droplet [blue spectrum, Fig. 5(b)] gives molecular-fingerprint Raman bands due to lipids at 1741 cm^{-1} (C=O stretching of ester), 1300 cm^{-1} (CH_2 twisting), and 1260 cm^{-1} (=C—H bending). The band due to cholesterol is also observed at a Raman shift of 710 cm^{-1}. On the other hand, the spectral profile at the nucleoli [red spectrum, Fig. 5(b)] shows characteristic bands due to nucleic acids at 1574 cm^{-1} (adenine and guanine), 1481 cm^{-1} (adenine and guanine), and 791 cm^{-1} (cytosine, thymine, and uracil).
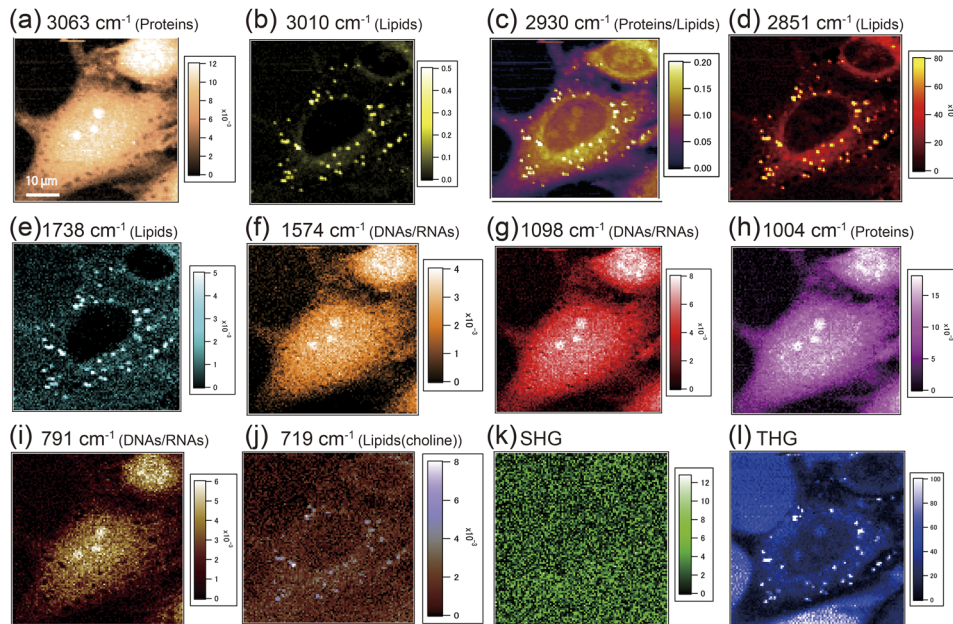
FIG. 4. CARS, SHG, and THG images of a HeLa cell in the G1 phase. CARS images at [(a)–(j)] 3063, 3010, 2930, 2851, 1738, 1574, 1098, 1004, 791, and 719 cm^{-1}, respectively, and the (k) SHG and (l) THG images.

We have also conducted a similar experiment for living NIH-3T3 cells (Fig. 6) with an exposure of 10 ms, which gives results similar to those obtained with HeLa cells. One of the intriguing differences is the clear contrast of the SHG image at the cell surface. Further investigation to elucidate the SHG-active molecular assembly at cell membranes is ongoing.

HeLa cells at the early stage of M phase

Next, we performed CARS imaging of a HeLa cell at the early stage of the M phase or prophase (chromosome condensation). Figure 7 shows multiplex CARS images for the same bands as in Fig. 4, along with the SHG and THG images. The SHG image [Fig. 7(k)] shows the presence of filament-like structures around the center of the cell. Based on the results of previous studies,[40,41] this organelle corresponds to spindle fibers. Moreover, clear vibrational contrast was found in the CARS images at 1574, 1098, and 791 cm^{-1} due to DNAs/RNAs, which represents chromosomes beginning to condense, indicating that the cell is in prophase. Similar to the results shown in Fig. 4, particle-like structures with diameters of a few micrometers are visible in Figs. 7(b)–7(e) and 7(l). As observed in
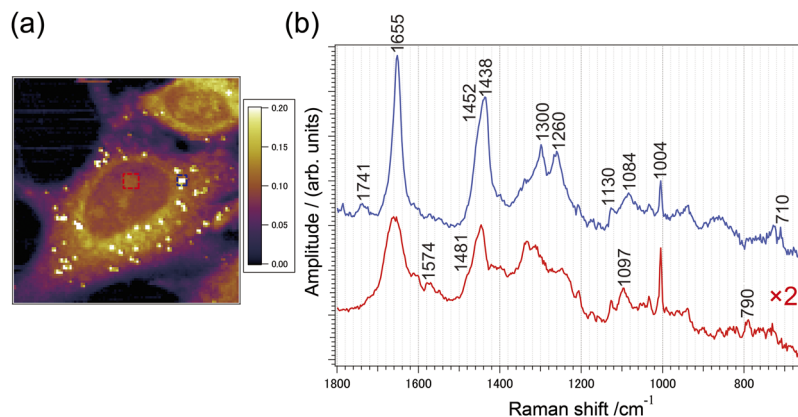

FIG. 5. (a) CARS image at 2930 cm^{-1}. (b) Im[$\chi^{(3)}$] spectra at areas marked by blue and red frames in (a).
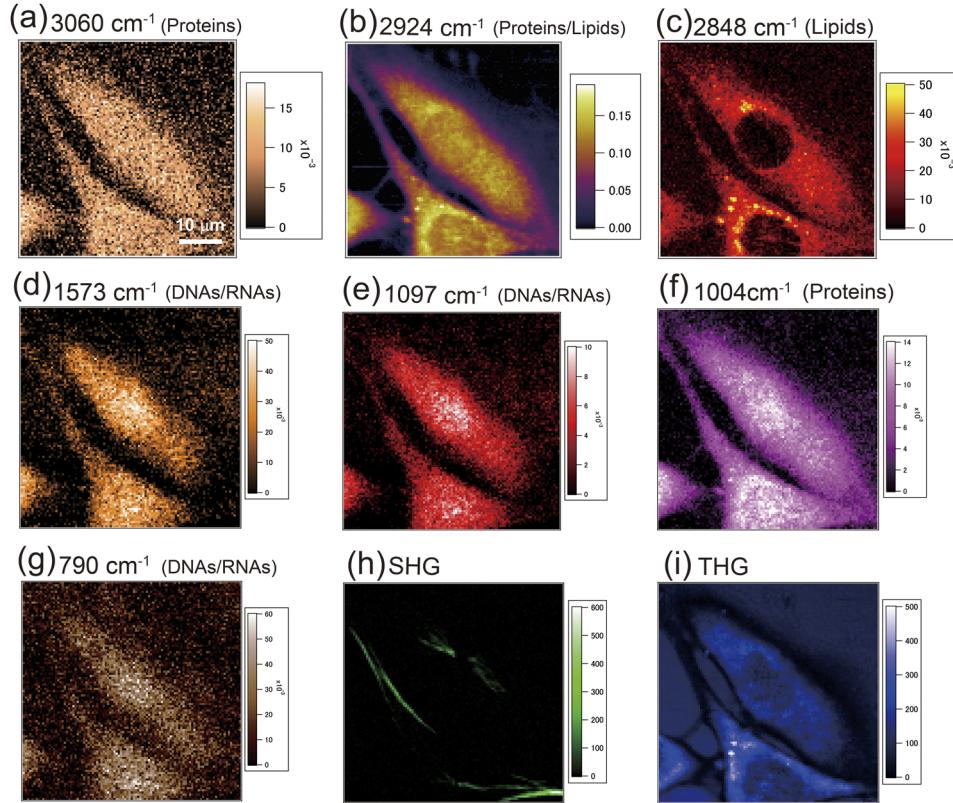
FIG. 6. CARS, SHG, and THG images of NIH-3T3 cells in the G1 phase with an exposure time of 10 ms. CARS images at [(a)–(g)] 3060, 2924, 2848, 1573, 1097, 1004, and 790 cm^{-1}, respectively, and the (h) SHG and (i) THG images.

the G1 phase, these particle-like structures are identified as lipid droplets. The lipid droplets in Fig. 7 also show distinct vibrational contrast with the band at 1004 cm^{-1} [Fig. 7(h)], which is attributable to proteins (the phenyl ring breathing mode). Since a recent study has shown that lipid droplets recruit
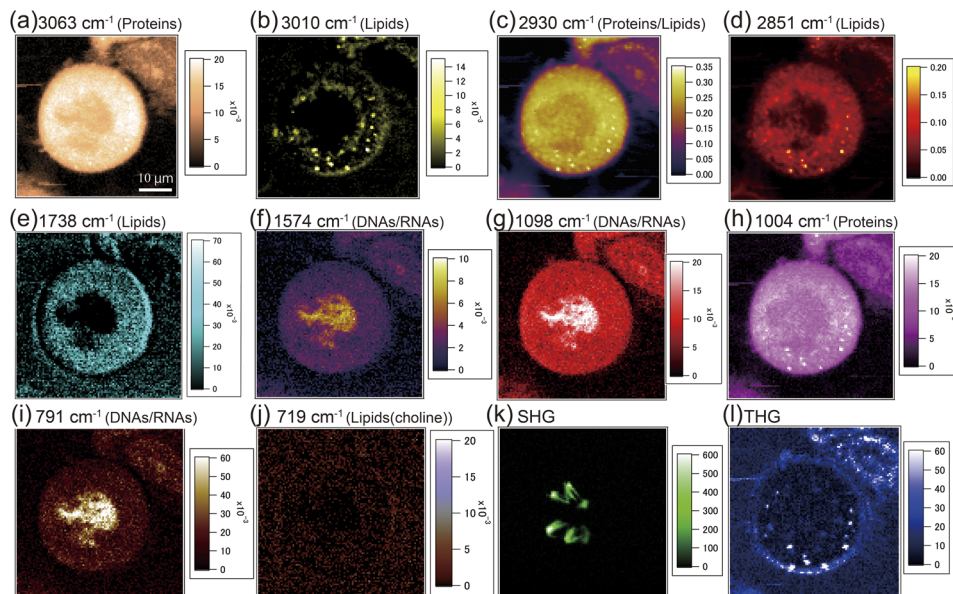

FIG. 7. CARS, SHG, and THG images of a HeLa cell in prophase. CARS images at [(a)–(j)] 3063, 3010, 2930, 2851, 1738, 1574, 1098, 1004, 791, and 719 cm^{-1}, respectively, and the (k) SHG and (l) THG images.

proteins from other cellular compartments in a cell type-specific and regulated manner,[42] the lipid droplets in Fig. 7 should be more involved in protein dynamics than those in Fig. 4.

In order to analyze the spatio-spectroscopic features in greater detail, we merged two images, i.e., that for the CARS signal at 791 cm^{-1} and that for the SHG signal, as shown in Fig. 8(a). The areas marked by light blue, red, and blue frames in Figs. 8(a) and 8(b) correspond to a spindle fiber, chromosome, and lipid droplet, respectively, the Im[$\chi^{(3)}$] spectra of which are shown in Fig. 8(c). The whole-cell-averaged Im[$\chi^{(3)}$] spectrum is also given by the black curve in Fig. 8(c). The overall spectral features of the whole-cell-averaged Im[$\chi^{(3)}$] spectrum are similar to those for the spectrum shown in Fig. 3, which is mainly attributable to proteins. This tendency is also visible in the spectral profile of the spindle fiber [light-blue curve, Fig. 8(c)] and even in that of the lipid droplet [blue curve, Fig. 8(c)]. In other words, the fingerprint Raman bands due to lipids are observed at 1741 cm^{-1} (C=O stretching of ester), 1300 cm^{-1} (CH$_2$ twist), 1260 cm^{-1} (=C—H bending), and 710 cm^{-1} (cholesterol); however, these bands were weaker than those for the lipid droplet in the G1 phase [Fig. 4(b)]. As discussed earlier, these lipid droplets are composed of lipids and proteins. On the other hand, the spectral profile at the chromosome shows clear fingerprint Raman bands due to nucleic acids at 1573 cm^{-1} (adenine and guanine), 1481 cm^{-1} (adenine and guanine), 1374 cm^{-1} (thymine, adenine, and cytosine), 1335 cm^{-1} (adenine and guanine), 1093 cm^{-1} (PO$_2^-$ stretching), and 790 cm^{-1} (cytosine, thymine, and uracil).

HeLa cells in M phase

Next, we performed CARS imaging of a HeLa cell in the M phase, in which mitotic cell division occurs. Figure 9 shows multiplex CARS images for the same bands, as in Figs. 4 and 7, along with the SHG and THG images. The CARS image obtained at 791 cm^{-1} [Fig. 9(i)] shows that the chromosomes are condensed and aligned at the metaphase plate. A merged image of the image for the CARS signal at 791 cm^{-1} and the SHG signal is shown in Fig. 10, which illustrates that the spindle fibers (SHG image) capture the chromosomes (CARS image at 791 cm^{-1}). Lipid-rich organelles are also visible in the CARS images in Figs. 9(b)–9(e), 9(j), and 9(l). One of the striking differences between Figs. 4, 7, and 9 is the clear vibrational contrast at the fingerprint Raman band of 719 cm^{-1}.

To investigate the molecular species in the lipid-rich areas in Figs. 4, 7, and 9, we analyzed the intracellular molecular-specific averaged spectra; the results are summarized in Fig. 11. Figures 11(a)–11(c) show the lipid-rich areas of Figs. 4, 7, and 9, respectively. These areas were chosen based on the amplitude of the =C—H stretching vibrational mode. We used this band for lipid imaging because it is located outside the congested fingerprint region, and its amplitude is sufficiently high
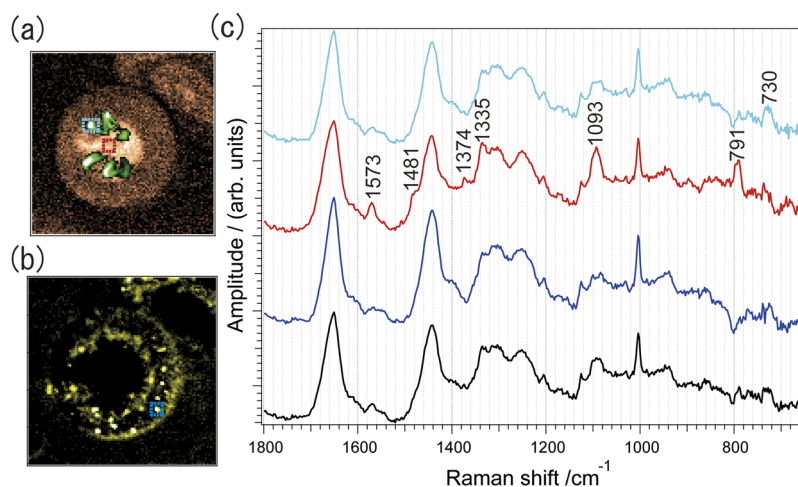

FIG. 8. (a) Merged image of the two images for the CARS signal at 791 cm^{-1} and the SHG signal. (b) CARS image at 3010 cm^{-1}. (c) Im[$\chi^{(3)}$] spectra at the light blue (spindle fiber), red (chromosome), and blue (particle-like structure) areas indicated in (a) and (b), and intracellular-averaged Im[$\chi^{(3)}$] spectrum (black).
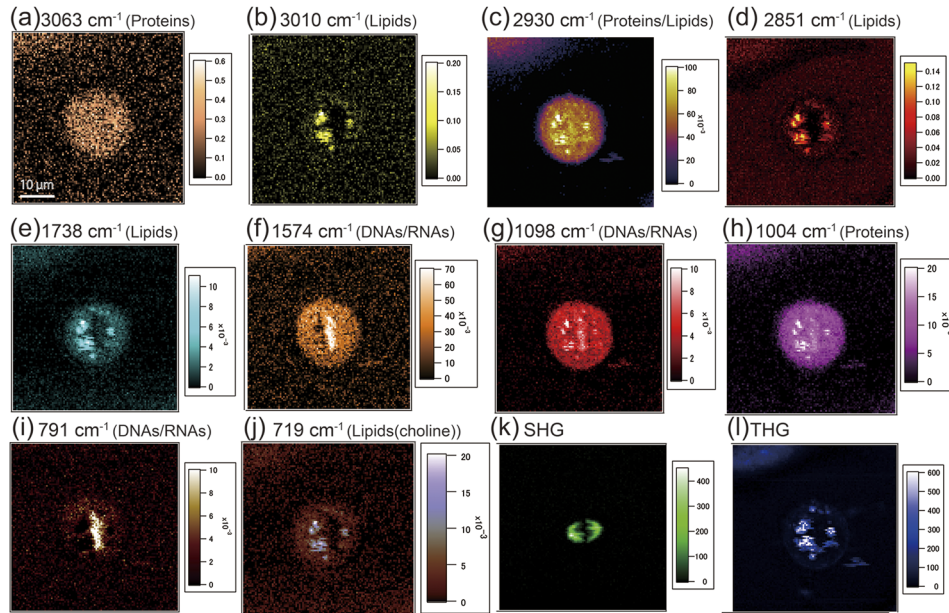
FIG. 9. CARS, SHG, and THG images of a HeLa cell in the M phase. CARS images at [(a)–(j)] 3063, 3010, 2930, 2851, 1738, 1574, 1098, 1004, 791, and 719 cm^{-1}, and the (k) SHG and (l) THG images.

for such a detailed analysis. As shown in Fig. 11(d), the fingerprint Raman band due to choline was found at the Raman shift of 719 cm^{-1}, which is the marker band for phosphatidylcholine (PC), which is a major component of phospholipid bilayer comprising membranous compartments such as the nuclear envelope, endoplasmic reticulum (ER), and Golgi network. Another marker band due to PC was also observed at the Raman shift of 1660 cm^{-1}, as a shoulder.[34] As metaphase is approached, the nuclear envelopes are disassembled[43] and fragmented,[44] followed by incorporation into ER.[45] Such membranous organelles, including Golgi apparatus, are accurately divided into daughter cells in accordance with the cell division axis.[46] Thus, the particle-like signal corresponding to PC in Fig. 9(j) most likely represents these membrane dynamics during mitosis.
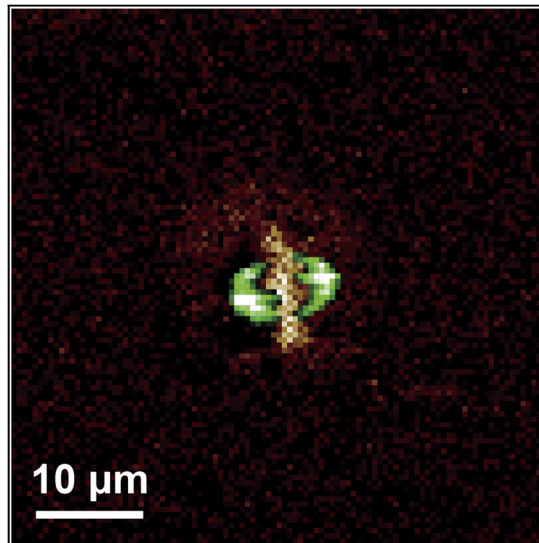

FIG. 10. Merged image of the two images for the CARS signal at 791 cm^{-1} and the SHG signal for a HeLa cell in the M phase.
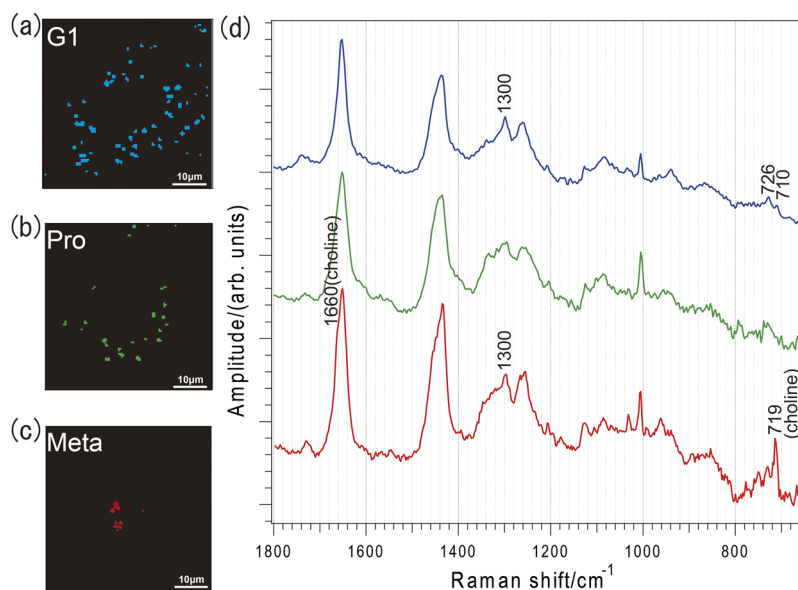
FIG. 11. Lipid-rich areas of Figs. 3(a) (blue), 5(b) (green), and 7(c) (red) highlighted using the amplitude of the =C−H stretching vibrational mode. The labels "Pro" and "Meta" correspond to prophase and M phase, respectively; (d) Im[$\chi^{(3)}$] spectra (blue, green, and red) averaged over lipid-rich areas labeled (a), (b), and (c), respectively, in the fingerprint region.

CONCLUSIONS

In conclusion, we developed a new CARS microspectroscopic system using a new laser source based on the MOFA configuration. The exposure time (pixel dwell time) was reduced to 0.8 ms, limited by the readout time of a CCD camera, due to the high peak power of the new laser source. Based on the clear molecular fingerprint, we successfully visualized intracellular molecular distribution with 10 vibrational bands. In particular, we determined that phospholipids are packaged in the M phase of a HeLa cell. This visualizing technique can be useful for understanding the dynamics of secretory and endosomal membrane trafficking that is important not only for interphase but also for mitotic accurate organelle inheritance including cytokinesis[44] and asymmetric cell division.[47] Thus, our label-free imaging presents considerable potential for mini- or non-invasive, real-time cellular-level molecular diagnostics for experimental and future clinical usages. After submission of this manuscript, Hashimoto *et al.* reported ultrabroadband Fourier-transform CARS spectroscopy covering over 3000 cm^{-1} at a scan rate of more than 10 000 spectra/s (Hashimoto *et al.*, Opt. Express **26**, 14307–14314 (2018)).

ACKNOWLEDGMENTS

[1] J. P. R. Day, K. F. Domke, G. Rago, H. Kano, H. Hamaguchi, E. M. Vartiainen, and M. Bonn, J. Phys. Chem. B **115**(24), 7713–7725 (2011).
[2] W. Min, C. W. Freudiger, S. J. Lu, and X. S. Xie, Annu. Rev. Phys. Chem. **62**, 507–530 (2011).
[3] C. Y. Chung, J. Boik, and E. O. Potma, Annu. Rev. Phys. Chem. **64**, 77–99 (2013).
[4] J.-X. Cheng and X. S. Xie, Science **350**(6264), aaa8870 (2015).
[5] C. S. Liao and J. X. Cheng, Annu. Rev. Anal. Chem. **9**(1), 69–93 (2016).
[6] H. Kano, H. Segawa, M. Okuno, P. Leproux, and V. Couderc, J. Raman Spectrosc. **47**(1), 116–123 (2016).
[7] J. X. Cheng, A. Volkmer, L. D. Book, and X. S. Xie, J. Phys. Chem. B **106**(34), 8493–8498 (2002).
[8] M. Muller and J. M. Schins, J. Phys. Chem. B **106**(14), 3715–3723 (2002).
[9] T. W. Kee and M. T. Cicerone, Opt. Lett. **29**(23), 2701–2703 (2004).

[10] H. Kano and H. Hamaguchi, Appl. Phys. Lett. **86**(12), 121113 (2005).
[11] G. I. Petrov and V. V. Yakovlev, Opt. Express **13**(4), 1299–1306 (2005).
[12] E. R. Andresen, H. N. Paulsen, V. Birkedal, J. Thogersen, and S. R. Keiding, J. Opt. Soc. Am. B **22**(9), 1934–1938 (2005).
[13] C. H. Camp, Jr., Y. J. Lee, J. M. Heddleston, C. M. Hartshorn, A. R. H. Walker, J. N. Rich, J. D. Lathia, and M. T. Cicerone, Nat. Photonics **8**, 627–634 (2014).
[14] C. W. Freudiger, W. Min, G. R. Holtom, B. Xu, M. Dantus, and X. S. Xie, Nat. Photonics **5**(2), 103–109 (2011).
[15] Y. Ozeki, W. Umemura, K. Sumimura, N. Nishizawa, K. Fukui, and K. Itoh, Opt. Lett. **37**(3), 431–433 (2012).
[16] D. Fu, F. K. Lu, X. Zhang, C. Freudiger, D. R. Pernik, G. Holtom, and X. S. Xie, J. Am. Chem. Soc. **134**(8), 3623–3626 (2012).
[17] Y. Ozeki, W. Umemura, Y. Otsuka, S. Satoh, H. Hashimoto, K. Sumimura, N. Nishizawa, K. Fukui, and K. Itoh, Nat. Photonics **6**(12), 845–851 (2012).
[18] C.-S. Liao, K.-C. Huang, W. Hong, A. J. Chen, C. Karanja, P. Wang, G. Eakins, and J.-X. Cheng, Optica **3**(12), 1377 (2016).
[19] J. P. Ogilvie, E. Beaurepaire, A. Alexandrou, and M. Joffre, Opt. Lett. **31**(4), 480–482 (2006).
[20] K. Hashimoto, M. Takahashi, T. Ideguchi, and K. Goda, Sci. Rep. **6**, 021036 (2016).
[21] A. S. Duarte, C. Schnedermann, and P. Kukura, Sci. Rep. **6**, 037516 (2016).
[22] T. Ideguchi, S. Holzner, B. Bernhardt, G. Guelachvili, N. Picque, and T. W. Hansch, Nature **502**(7471), 355–358 (2013).
[23] M. Okuno, H. Kano, P. Leproux, V. Couderc, J. P. R. Day, M. Bonn, and H. Hamaguchi, Angew. Chem., Int. Ed. **49**(38), 6773–6777 (2010).
[24] K. Isobe, A. Suda, M. Tanaka, H. Hashimoto, F. Kannari, H. Kawano, H. Mizuno, A. Miyawaki, and K. Midorikawa, Opt. Express **17**(14), 11259–11266 (2009).
[25] W. Langbein, I. Rocha-Mendoza, and P. Borri, Appl. Phys. Lett. **95**(8), 081109 (2009).
[26] M. Okuno, H. Kano, P. Leproux, V. Couderc, and H. Hamaguchi, Opt. Lett. **32**(20), 3050–3052 (2007).
[27] R. Vlijm, X. Li, M. Panic, D. Ruthnick, S. Hata, F. Herrmannsdorfer, T. Kuner, M. Heilemann, J. Engelhardt, S. W. Hell, and E. Schiebel, Proc. Natl. Acad. Sci. U. S. A. **115**(10), E2246–E2253 (2018).
[28] T. Akiyama, A. Inoko, Y. Kaji, S. Yonemura, K. Kakiguchi, H. Segawa, K. Ishitsuka, M. Yoshida, O. Numata, P. Leproux, V. Couderc, T. Oshika, and H. Kano, Sci. Rep. **7**, 039967 (2017).
[29] E. Capitaine, N. O. Moussa, C. Louot, S. M. Bardet, H. Kano, L. Duponchel, P. Leveque, V. Couderc, and P. Leproux, Biomed. Opt. Express **9**(1), 245–253 (2018).
[30] E. M. Vartiainen, H. A. Rinia, M. Müller, and M. Bonn, Opt. Express **14**, 3622–3630 (2006).
[31] T. Shimanouchi, J. Phys. Chem. Ref. Data **6**(3), 993–1102 (1977).
[32] Q. Matthews, A. Brolo, J. Lum, X. Duan, and A. Jirasek, Phys. Med. Biol. **56**(1), 19–38 (2011).
[33] M. T. Cicerone and C. H. Camp, Analyst **143**(1), 33–59 (2017).
[34] C. Krafft, L. Neudert, T. Simat, and R. Salzer, Spectrochim. Acta, Part A **61**(7), 1529–1535 (2005).
[35] B. W. Barry, H. G. M. Edwards, and A. C. Williams, J. Raman Spectrosc. **23**(11), 641–645 (1992).
[36] H. Deng, V. A. Bloomfield, J. M. Benevides, and G. J. Thomas, Biopolymers **50**(6), 656–666 (1999).
[37] R. G. Snyder, H. L. Strauss, and C. A. Elliger, J. Phys. Chem. **86**(26), 5145–5150 (1982).
[38] R. G. Snyder and J. R. Scherer, J. Chem. Phys. **71**(8), 3221–3228 (1979).
[39] K. G. Brown, E. Bicknell-Brown, and M. Ladjadj, J. Phys. Chem. **91**(12), 3436–3442 (1987).
[40] P. J. Campagnola, M. D. Wei, A. Lewis, and L. M. Loew, Biophys. J. **77**(6), 3341–3349 (1999).
[41] S. Bancelin, C. A. Couture, M. Pinsard, M. Rivard, P. Drapeau, and F. Legare, Sci. Rep. **7**(1), 6758 (2017).
[42] M. A. Welte, Trends Cell Biol. **17**(8), 363–369 (2007).
[43] M. W. Hetzer, Cold Spring Harbor Perspect. Biol. **2**(3), a000539 (2010).
[44] G. W. Gould and J. Lippincott-Schwartz, Nat. Rev. Mol. Cell Biol. **10**, 287 (2009).
[45] L. Champion, M. I. Linder, and U. Kutay, Trends Cell Biol. **27**(1), 26–41 (2017).
[46] M. L. Jongsma, I. Berlin, and J. Neefjes, Trends Cell Biol. **25**(3), 112–124 (2015).
[47] P. Gonczy, Nat. Rev. Mol. Cell Biol. **9**(5), 355–366 (2008).